10-22-2021

High-Entropy Alloys Properties Prediction Model by Using Artificial Neural Network Algorithm

Sanggyu Choi
Department of Materials Science and Engineering, Inha University, 100 Inha-ro, Michuhol-Gu, Incheon 22212, Korea

Sung Yi
Portland State University, syi@pdx.edu

Junghan Kim
Department of Materials Science and Engineering, Inha University, 100 Inha-ro, Michuhol-Gu, Incheon 22212, Korea

Byungsue Shin
Department of Materials Science and Engineering, Inha University, 100 Inha-ro, Michuhol-Gu, Incheon 22212, Korea

Soongkeun Hyun
Department of Materials Science and Engineering, Inha University, 100 Ienha-ro, Michuhol-Gu, Incheon 22212, Korea

Citation Details

Article

High-Entropy Alloys Properties Prediction Model by Using Artificial Neural Network Algorithm

Sanggyu Choi [1], Sung Yi [2], Junghan Kim [1], Byungsue Shin [1] and Soongkeun Hyun [1,*

[1] Department of Materials Science and Engineering, Inha University, 100 Inha-ro, Michuhol-Gu, Incheon 22212, Korea; sanggyuchoi@inha.edu (S.C.); jhkim2292@inha.ac.kr (J.K.); kzzsc@naver.com (B.S.)
[2] Department of Mechanical and Materials Engineering, Portland State University, Portland, OR 97207-0751, USA; syi@pdx.edu
*** Correspondence: skhyun@inha.ac.kr; Tel.: +82-32-850-0215

Abstract: A new approach method has been studied for the efficient and accurate prediction of high-entropy alloys (HEAs) properties. The artificial neural network (ANN) algorithm was employed to predict the mechanical properties such as yield strength, microstructure, and elongation of the alloy by training from the mole fraction and post-process information that has an influence on the mechanical properties. The mean error rate of prediction for the yield strength was 19.6%. Microstructure predictions were consistent for all test data. On the other hand, the ANN model trained only with mole fraction data had a yield strength prediction error of 33.9%. Omission of post-process data caused a decrease in the accuracy. In addition, the prediction was performed with the lasso regression model in the same way. The mean error rate of the lasso model trained with only a mole fraction was 26.1%. The lasso model trained with a mole fraction and post-process data had a yield strength prediction error of 31.1%. The linear regression equation showed limitations, as the accuracy decreased as the number of independent variables increased. As there are more variables affecting metal properties, the ANN approach is more advantageous, and the more data there are, the more accuracy increases, making it possible to design HEAs alloys that are simpler and more efficient than conventional methods. This approach predicted HEAs properties using only mole fraction and post-processing information, without the need to use conventional physicochemical theories or perform derived complex calculations.

Keywords: prediction; properties; high-entropy alloys; yield strength; microstructure; artificial neural network

1. Introduction

High-entropy alloys (HEAs) are alloys that are formed by mixing equal or relatively large proportions of usually five or more elements. HEAs systems are in contrast to traditional alloys, which contain just one or two primary constituent chemical species. As a result of their unique microstructure and properties, these HEAs have attracted the research interest of the scientific community and have been under development. However, there are thousands of combinations for experiments with all elements including mole fractions. It is impossible to carry out experiments in all cases. An empirical design through trial and error has been replaced by computer-based alloy designs. In terms of the formulation and accuracy of the predictive model, most of it comes from experimental data, which requires a significant amount of experimental input. HEAs have been generally known to require high entropy to obtain a stable phase of a single solid solution [1]. Atomic size mismatch, mixed enthalpy, valence electron concentration, and thermodynamic parameters have been studied for the purpose of predicting these HEA properties [2–5]. The calculation of phase diagram (CALPHAD) which consists of thermodynamic databases from extensive experimental and thermodynamic calculations based on Gibbs free energy has been studied [6–8]. The molecular dynamics simulation method also has been used to

predict alloy properties [9]. The method of predicting properties through thermodynamic calculations requires calculating various indices that determine HEA properties such as the parameters of the entropy of mixing, enthalpy of mixing, atomic size difference, valence electron concentration, Allen, and Pauling electronegativity every time the component ratio changes [10]. However, these methods do not always derive accurate results. In addition, calculations require exclusive software or equipment.

In this study, based on the ANN algorism, we propose an efficient framework for selecting the optimal component elements and post-process conditions in the most important step, HEA design. Research on efficient alloy design by machine learning has been performed. Manzoor et al. [11] used machine learning and density functional theory calculations to predict the vibrational entropy of FCC solids and reduce complex computations. Zhang et al. [12] studied the prediction accuracy of the phase formation problem of HEAs using genetic algorithms. Pei et al. [13] predicted 93% of the formation of the solid solution by machine learning. HEA is being studied not only in the metallurgical industry but also in the medical field because of its superior properties such as high strength, high ductility, corrosion resistance, and thermal stability compared to other alloys [14–16]. If the mole fraction of elements and process conditions required to obtain the properties of HEA can be known in advance, the number of experiments can be reduced in the design stage. As input data for ANN learning, mole fraction and post-process data were used. In order to improve the model prediction performance even with a small dataset, the accuracy was verified through the model optimization process. The ANN prediction model showed a similar prediction tendency to the linear regression method compared to the lasso regression model, and the effects of variables on the alloy properties were compared. As the number of variables and data increased, the ANN prediction model made more accurate predictions. This methodology greatly simplifies calculation and opens a new way to predict the properties of HEA with less data, which can be utilized to predict properties in advance through alloy design.

2. Methodology

2.1. HEAs Data Information

From the reference [9,14–37], the experimental data for various HEAs were collected to train the model for predicting HEA characteristics. The collected data are mole fraction, post-process information, yield strength, phase, and elongation. There are two groups of HEA: the refractory metal group consisting of Al, Hf, Nb, Ta, Ti, Zr, V, Mo, and W, and the transition group containing Al, Co, Cr, Fe, Ni, Cu, and Mn. All data were obtained after the casting process. Post-process data were arranged in order heat treatment, cooling condition, cold-roll conditions, hot-roll conditions, heat treatment, forging condition, hot isostatic pressing (HIP) conditions, and heat treatment. For the post-process that did not proceed, the 0 value was put. The reason that the heat treatment condition is in three columns is that there are cases in which heat treatment is performed after each post-process is finished. These post-process and mole fraction data were used as input data for training the ANN prediction model. Yield strength, elongation, and microstructure were set as the output data to predict. The training data set was a total of 36 data. After the model was derived, 8 test data were used to evaluate the accuracy of metal group data. All data are shown in Table 1.

Table 1. Collected data set of high-entropy alloys mole fraction with post-process conditions and properties results data used for input and output in an artificial neural network prediction model.

No., [Ref]	Alloy	Al	Co	Cr	Fe	Ni	Cu	Mn	Hf	Nb	Ta	Ti	Zr	V	Mo	W	σ^y *(MPa)	Phase	ε **(%)
1, [9]***	$NbCrMo_{0.5}Ta_{0.5}TiZr$	0	0	20	0	0	0	0	0	20	10	20	20	0	10	0	1595	FCC	5
2, [14]	$Al_{0.5}CoCrCu_{0.5}FeNi_2$	8.3	16.7	16.7	16.7	33.3	8.3	0	0	0	0	0	0	0	0	0	215	BCC	39
3, [15]	$Al_{0.5}CoCrCFeNi$	9.1	18.2	18.2	18.2	18.2	18.2	0	0	0	0	0	0	0	0	0	360	BCC	19
4, [16]	$AlNbTiV$	25	0	0	0	0	0	0	0	25	0	25	0	25	0	0	1020	FCC	5
5, [9]	$NbCrMo_{0.5}Ta_{0.5}TiZr$	0	0	20	0	0	0	0	0	20	10	20	20	0	10	0	1595	FCC	5
6, [18]	$Al_{0.5}NbTaTiV$	11.1	0	0	0	0	0	0	0	22.2	22.2	22.2	0	22.2	0	0	1012	FCC	50
7, [19]	$CoCrFeNi$	0	25	25	25	25	0	0	0	0	0	0	0	0	0	0	273	BCC	38
8, [20]	$AlCoCrCuFeNi$	16.7	16.7	16.7	16.7	16.7	16.7	0	0	0	0	0	0	0	0	0	1040	BCC + FCC	1
9, [21]	$Al_{0.3}CoCrFeNi$	7.0	23.3	23.3	23.3	23.3	0	0	0	0	0	0	0	0	0	0	224	BCC	48
10, [22]	$MoNbTaVW$	0	0	0	0	0	0	0	0	20	20	0	0	20	20	20	1246	FCC	1.7
11, [23]	$Al_{0.5}CrCuFeNi_2$	9.1	0	18.2	18.2	36.4	18.2	0	0	0	0	0	0	0	0	0	704	BCC + FCC	5.6
12, [24]	$CrHfNbTiZr$	0	0	20	0	0	0	0	20	20	0	20	20	0	0	0	1375	FCC	2.8
13, [21]	$Al_{0.3}CoCrFeNi$	7.0	23.3	23.3	23.3	23.3	0	0	0	0	0	0	0	0	0	0	310	BCC	44
14, [25]	$NbTiVZr$	0	0	0	0	0	0	0	0	20	0	20	20	40	0	0	918	FCC	50
15, [26]	$CrCrFeMnNi$	0	20	20	20	20	0	20	0	0	0	0	0	0	0	0	171	BCC	57
16, [27]	$Al_{0.3}NbTaTi_{1.4}Zr_{1.3}$	6	0	0	0	0	0	0	0	20	20	28	26	0	0	0	1965	FCC	5
17, [21]	$Al_{0.3}CoCrFeNi$	7.0	23.3	23.3	23.5	23.5	0	0	0	0	0	0	0	0	0	0	240	BCC	45
18, [19]	$CoCrMnNi$	0	25	25	0	25	0	25	0	0	0	0	0	0	0	0	280	BCC	43
19, [18]	$AlNbTaTiV$	20	0	0	0	0	0	0	0	20	20	20	0	20	0	0	991	FCC	50
20, [24]	$HfNbTiVZr$	0	0	0	0	0	0	0	20	20	0	20	20	20	0	0	1170	FCC	30
21, [28]	$HfNbTaTiZr$	0	0	0	0	0	0	0	20	20	20	20	20	0	0	0	1145	FCC	9.7
22, [26]	$CrFeMnNi$	0	20	20	20	20	0	20	0	0	0	0	0	0	0	0	362	BCC	51
23, [25]	$CrNbTiZr$	0	0	25	0	0	0	0	0	25	0	25	25	0	0	0	1260	FCC	6
24, [29]	$CoCrFeNi$	0	25	25	25	25	0	0	0	0	0	0	0	0	0	0	300	BCC	42
25, [30]	$AlMo_{0.5}NbTa_{0.5}TiZr$	20	0	0	0	0	0	0	0	20	10	20	20	0	10	0	2000	FCC	1
26, [31]	$HfMoNbTiZr$	0	0	0	0	0	0	0	20	20	0	20	20	0	20	0	1575	FCC	9
27, [32]	$CrFeMnNi$	0	20	20	20	20	0	20	0	0	0	0	0	0	0	0	410	BCC	57
28, [20]	$AlCoCrCuFeNi$	16.7	16.7	16.7	16.7	16.7	16.7	0	0	0	0	0	0	0	0	0	790	BCC + FCC	0.2
29, [23]	$Al_{0.5}CrCuFeNi_2$	9.1	0	18.2	18.2	16.4	18.2	0	0	0	0	0	0	0	0	0	630	BCC + FCC	4.2
30, [27]	$Al_{0.5}NbTa_{0.8}Ti_{1.5}V_{0.2}Zr$	10	0	0	0	0	0	0	0	20	16	30	20	4	0	0	2035	FCC	4.5
31, [18]	$Al_{0.25}NbTaTiV$	5.9	0	0	0	0	0	0	0	23.5	23.5	23.5	0	23.5	0	0	1330	FCC	50
32, [14]	$Al_{0.5}CoCrCu_{0.5}FeNi_2$	8.3	16.7	16.7	16.7	33.3	8.3	0	0	0	0	0	0	0	0	0	357	BCC	9
33, [33]	$HfNbTiZr$	0	0	0	0	0	0	0	25	25	0	25	25	0	0	0	879	FCC	14.9
34, [22]	$MoNbTaW$	0	0	0	0	0	0	0	0	25	25	0	0	0	25	25	1058	FCC	2.6
35, [34]	$NbTaTiV$	0	0	0	0	0	0	0	0	25	25	25	0	25	0	0	1092	FCC	50
36, [27]	$AlNb_{1.5}Ta_{0.5}Ti_{1.5}Zr_{0.5}$	20	0	0	0	0	0	0	0	30	10	30	10	0	0	0	1280	FCC	3.5
1t****, [35]	$Al_{0.5}CoCrCuFeNi$	9.1	18.2	18.2	18.2	18.2	18.2	0	0	0	0	0	0	0	0	0	1284	BCC	7.6
2t, [26]	$CrFeMnNi$	0	20	20	20	20	0	20	0	0	0	0	0	0	0	0	197	BCC	60
3t, [27]	$Al_{0.3}NbTa_{0.8}Ti_{1.4}V_{0.2}Zr_{1.3}$	6	0	0	0	0	0	0	0	20	16	28	26	4	0	0	1965	FCC	5
4t, [25]	$CrNbTiVZr$	0	0	20	0	0	0	0	0	20	0	20	20	20	0	0	1298	FCC	3
5t, [19]	$CoFeMnNi$	0	25	0	25	25	0	25	0	0	0	0	0	0	0	0	175	BCC	41
6t, [25]	$NbTiVZr$	0	0	0	0	0	0	0	0	25	0	25	25	25	0	0	1105	FCC	50
7t, [30]	$Al_{0.4}Hf_{0.6}NbTaTiZr$	8	0	0	0	0	0	0	12	20	20	20	20	0	0	0	1841	FCC	10
8t, [36]	$Al_{0.5}CoCrCuFeNi$	9.1	18.2	18.2	18.2	18.2	18.2	0	0	0	0	0	0	0	0	0	655	BCC	29

No., [Ref]	Heat Treatment 1 Temp (°C)	h	Cooling WQ	SC	CR (%)	HR Temp (°C)	HR (%)	Heat Treatment 2 Temp (°C)	h	Forge	HIP Temp (°C)	Press (MPa)	h	Heat Treatment 3 Temp (°C)	h
1, [9]	0	0	0	0	0	0	0	0	0	0	1450	207	2	1200	24
2, [14]	1150	5	1	0	0	0	0	0	0	0	0	0	0	0	0
3, [15]	0	0	0	0	0	0	0	0	0	0	0	0	0	0	0
4, [16]	1200	24	0	0	0	0	0	0	0	0	0	0	0	0	0
5, [9]	0	0	0	0	0	0	0	0	0	0	1200	207	2	1200	24
6, [18]	0	0	0	0	0	0	0	0	0	0	0	0	0	0	0
7, [19]	1200	24	0	0	92	0	0	1000	1	0	0	0	0	0	0
8, [20]	960	50	0	0	0	0	0	0	0	1	0	0	0	0	0
9, [21]	0	0	0	0	0	0	0	0	0	0	0	0	0	0	0
10, [22]	0	0	0	0	0	0	0	0	0	0	0	0	0	0	0
11, [23]	0	0	0	0	43	0	0	900	24	0	0	0	0	0	0
12, [24]	0	0	0	0	0	0	0	0	0	0	0	0	0	0	0
13, [21]	700	72	0	0	0	0	0	0	0	0	0	0	0	0	0
14, [25]	0	0	0	0	0	0	0	0	0	0	1200	207	2	1200	24
15, [26]	1200	48	0	0	87	0	0	1150	1	0	0	0	0	0	0
16, [27]	0	0	0	0	0	0	0	0	0	0	1200	207	2	1200	24
17, [21]	900	72	0	0	0	0	0	0	0	0	0	0	0	0	0
18, [19]	1100	24	0	0	90	0	0	1000	1	0	0	0	0	0	0
19, [18]	0	0	0	0	0	0	0	0	0	0	0	0	0	0	0
20, [24]	0	0	0	0	0	0	0	0	0	0	0	0	0	0	0
21, [28]	0	0	0	0	90	0	0	1000	2	0	1200	207	2	1200	24
22, [26]	1200	48	0	0	87	0	0	800	1	0	0	0	0	0	0
23, [25]	0	0	0	0	0	0	0	0	0	0	1200	207	2	1200	24
24, [29]	1000	24	0	0	0	1000	92	900	1	0	0	0	0	0	0
25, [30]	0	0	0	0	0	0	0	0	0	0	1400	207	2	1400	24
26, [31]	1100	10	0	1	0	0	0	0	0	0	0	0	0	0	0
27, [32]	0	0	0	0	60	0	0	800	1	1	0	0	0	0	0
28, [20]	0	0	0	0	0	0	0	0	0	0	0	0	0	0	0
29, [23]	0	0	0	0	43	0	0	700	24	0	0	0	0	0	0
30, [27]	0	0	0	0	0	0	0	0	0	0	1200	207	2	1200	24
31, [18]	0	0	0	0	0	0	0	0	0	0	0	0	0	0	0
32, [14]	0	0	0	0	0	0	0	0	0	0	0	0	0	0	0
33, [33]	1300	6	0	0	0	0	0	0	0	0	0	0	0	0	0
34, [22]	0	0	0	0	0	0	0	0	0	0	0	0	0	0	0
35, [34]	0	0	0	0	0	0	0	0	0	0	0	0	0	0	0
36, [27]	0	0	0	0	0	0	0	0	0	0	1400	207	2	1400	24
1t, [35]	1000	0	0	0	84	0	0	900	5	0	0	0	0	0	0
2t, [26]	1200	48	0	0	87	0	0	1000	1	0	0	0	0	0	0
3t, [27]	0	0	0	0	0	0	0	0	0	0	1200	207	2	1200	24
4t, [25]	0	0	0	0	0	0	0	0	0	0	1200	207	2	1200	24
5t, [19]	1100	24	0	0	90	0	0	1000	1	0	0	0	0	0	0
6t, [25]	0	0	0	0	0	0	0	0	0	0	1200	207	2	1200	24
7t, [30]	0	0	0	0	0	0	0	0	0	0	1200	207	2	1200	24
8t, [36]	1000	6	0	0	80	0	0	900	5	0	0	0	0	0	0

* yield strength. ** elongation. *** reference number. **** test data.

2.2. Data Preprocessing and Model Evaluation

From the collected data, three ANN models were derived based on three result data such as yield strength, microstructure, and elongation. These are the alloy properties that are basic information of metal alloy to use in mechanical systems. The three models are independent models because each model has different weights and biases even though they are using same input data. Yield strength and elongation prediction models are predicting the results as numeric. The output of the microstructure phase was encoded according to FCC, BCC, and FCC + BCC. When predicting the microstructure phase, the results were expressed as probabilistic using the softmax algorithm. All data have been normalized to a range of 0–1 with a maximum of 1 and a minimum of 0. Normalizing is expressed as shown in Equation (1).

$$X_i^{norm} = \frac{X_i - X_{min}}{X_{max} - X_{min}} \tag{1}$$

where X_{max} and X_{min} are the maximum and minimum values of descriptor X of our training data, respectively.

A mean square error (*MSE*) was used to estimate the accuracy of the prediction model. Until *MSE* value is minimized through a training data set, weights and biases are updated repeatedly. *MSE* is expressed as in Equation (2).

$$\min MSE = \frac{1}{n} \sum_{i=1}^{n} (y_i - \hat{y}_i)^2 \tag{2}$$

where y_i is measured output data from the result of alloy analysis in previous research. $\hat{y}_i$ is a calculated output data from the prediction model. i is the test number in Tables 1–3.

Table 2. Particular parameter used in artificial neural network prediction model on all layers.

Layer	Parameter	
Input data	Post-process Mole fraction	15 conditions 15 elements
Hidden layer 1	Node Activation function Optimizer	3 ReLU Adam
Hidden layer 2	Node Activation function Optimizer	47 ReLU Adam
Output layer	Node Activation function Optimizer	1 Regression, Softmax (phase) Adam
Results	Yield strength Microstructure phase Elongation	

Table 3. The prediction results of high-entropy alloy phases.

Input Data	1 Test Data	2 Test Data	3 Test Data	4 Test Data	5 Test Data	6 Test Data	7 Test Data	8 Test Data
Observed Phase	(1, 0) *	(1, 0)	(0, 1) **	(0, 1)	(1, 0)	(0, 1)	(0, 1)	(1, 0)
Predicted Phase	(1, 0)	(1, 0)	(0, 1)	(0, 1)	(1, 0)	(0, 1)	(0, 1)	(1, 0)
Accord/ Discord	Accord	Accord	Accord	Accord	Accord	Accord	Accord	Accord

* BCC (body-centered cubic). ** FCC (face-centered cubic).

Optimization Process for ANN Prediction Model

A total of 36 input data that consist of a mole fraction and post-process information are used as input data. When the hidden layer of the model was one layer, the model was

evaluated by increasing the number of nodes from 1 to 100 by 1. In the case of two hidden layers, the model was evaluated by increasing the number of nodes from 1 to 50 by 1 in each layer. The results of the two models were evaluated by recording the *MSE* value and mean error value. The results of the model optimization process are shown in Figure 1.
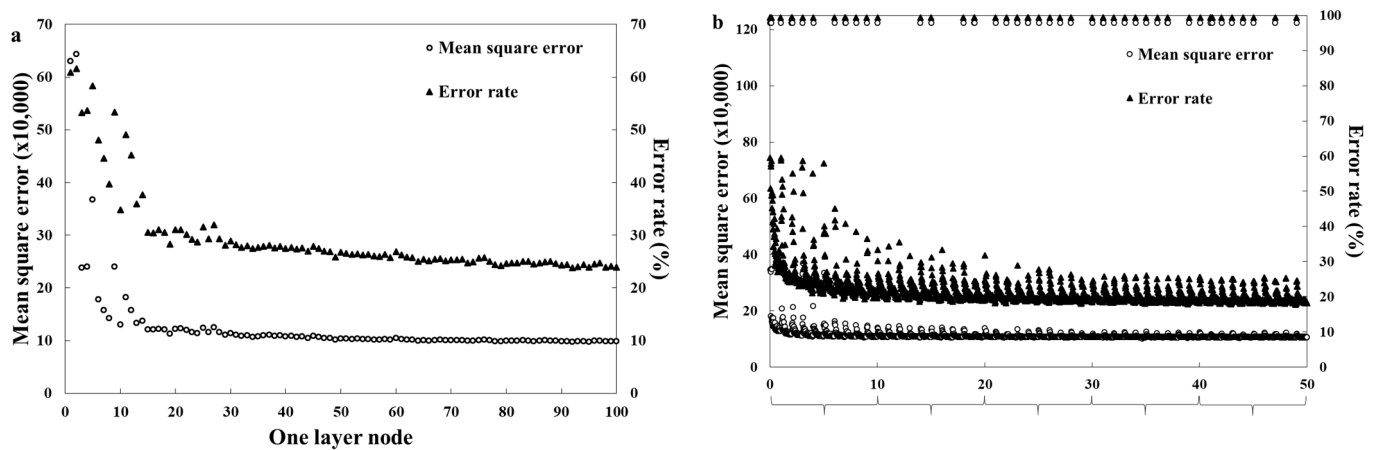

Figure 1. Accuracy change according to the number of nodes. (**a**) In the case of one hidden layers; (**b**) In the case of two hidden layers.

An optimal model size should be found in the ANN model to get an accurate prediction model. For the ANN model with one hidden layer, the *MSE* value decreased as the number of nodes increased. The *MSE* value converges to 11,000 when the number of nodes is more than 40. The average error rate converges to a value of 24% after 60 nodes. For ANN models with two hidden layers, the accuracy increases rapidly even with a small increase in the number of nodes, regardless of a node number in the first or second layer. The *MSE* value converges to 100,000, and the mean error converges to 20%. The optimized layer size representing the minimum mean error was (3, 47). The model training process involves choosing the gradient descent optimizer and the type of activation function to find the optimal parameters. In this study, an Adam optimizer was used that was introduced by Diederik P. [37]. Features are a fast search for optimal parameters and high accuracy. ReLU was used as the activation function. ReLU is an activation function for deep neural network algorithms. The parameter values applied to the ANN algorithm are given in Table 2.

2.3. Optimization Process for Lasso Linear Regression Prediction Model

A conventional linear regression is described as shown in Equation (3).

$$\hat{y} = w[0] \cdot X[0] + w[1] \cdot X[1] + \cdots + w[n] \cdot X[n] + b \tag{3}$$

where $w[0–n]$ is the weights to multiply to each independent variable $X[0–n]$. b is a constant called the bias. Each independent variable is multiplied by a weight and added a bias. The calculated prediction result is compared with the actual measurement result by the *MSE* equation of loss function. The purpose is to find the parameter that minimizes the *MSE* value through gradient descent. For higher accuracy, these calculations are iteratively calculated to find the optimal parameters of the weights and bias values.

The lasso regression finds the optimal parameters of weight and bias by imposing an L1-norm penalty on the MES equation. This penalty allows the sum of the absolute values of the weights to be minimized so that the weight of a particular independent variable can be zero. Therefore, the influence of the independent variable term that does not have a large effect on a dependent variable is ignored. At this time, the effect of the penalty is adjusted by multiplying the α-constant. In this study, α was set to 0.01. The number

of lessons was 10,000. The formula to which we added the L1-norm penalty is given in Equation (4).

$$\min MSE = \frac{1}{n}\sum_{i=1}^{n}(y - \hat{y})^2 + \alpha \sum_{j=1}^{m}|w_j| \tag{4}$$

where w_j is the weight value, and α is the constant. When the α value is increased, more weights values are zero. In this study, the α value was set at 0.01.

3. Results and Discussion

3.1. Evaluation Predicting Accuracy of ANN Models

Figure 2 shows the prediction results of the ANN model trained by mole fraction and post-process information for eight test data. The mean error rate of yield strength on the test data excluding the training data was 19.6%. The average difference was 205 MPa, and the coefficient of determination was 0.9068. In the elongation model, the mean error was 40.2%, the mean difference was 4.3%, and the coefficient of determination for all data predictions was 0.7950. Yield strength had high accuracy in the prediction of mechanical properties of HEAs than elongation prediction results. This low accuracy for elongation was no different in result between the model trained by all input data and the model trained by only mole fraction data. As for the elongation, the accuracy of prediction was low because there was a difference in the result value depending on the shape of the specimen to be measured or the measurement method. In order to accurately predict the elongation in the future, unification of the measurement method and more independent variables affecting elongation are needed. The results of the microstructure were accurately predicted for all data. The BCC, FCC, and BCC + FCC phases were encoded to (1, 0), (0, 1), and (1, 1) each. The result is shown in Table 3.
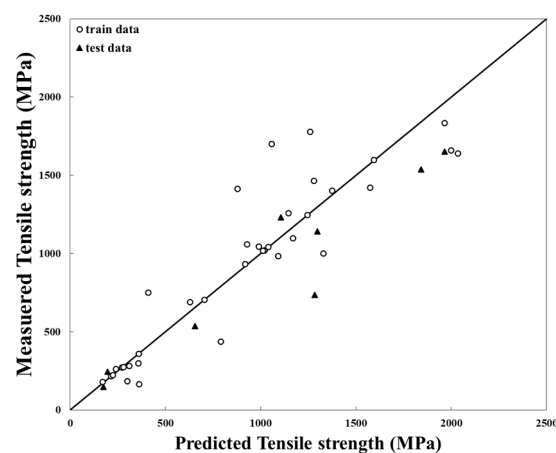

Figure 2. Accuracy of an ANN model trained with elemental mole fraction and process data.

Figure 3 shows the accuracy of an ANN model trained only on mole fraction information. For the yield strength prediction, the mean error was 33.9%. The mean difference was 241 MPa, and the coefficient of determination was 0.8117. Compared with the results in Figure 2, it had a higher accuracy of prediction results than the model trained with only the mole fraction information. In addition to HEA, existing alloys and metals have a post-process to control the mechanical properties. Even data having the same mole fraction show different mechanical properties depending on the post-process conditions. These facts influenced the accuracy of the model regarding data. The yield strength prediction results of eight test data calculated from both ANN models are given in Table 4.
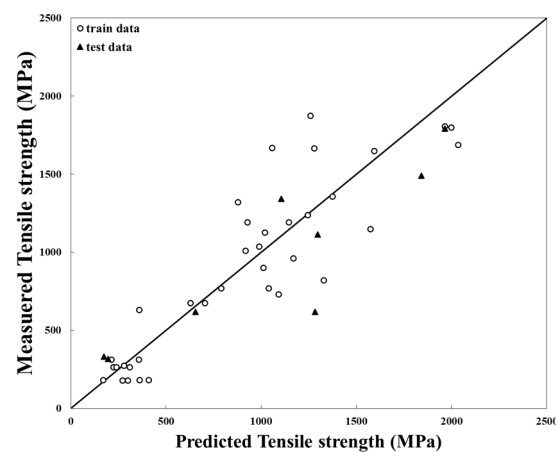
Figure 3. Accuracy of an ANN model trained only on elemental mole fractions.

Table 4. Comparison of the predicted results data calculated by the ANN model, which was trained on post-process and mole fraction data vs. mole fraction data.

No., [Ref]	HEA Group	σ_y^m * (MPa)	ANN Model Trained from Post-Process and Mole Fraction			ANN Model Trained from Mole Fraction		
			σ_y^p ** (MPa)	Error (MPa)	Error Rate (%)	σ_y^p ** (MPa)	Error (MPa)	Error Rate (%)
1, [35]	Transition	1284	735	549	42.8	617	667	52.0
2, [25]	Transition	197	244	47	24.0	317	120	60.9
3, [26]	Refractory	1965	1651	314	16.0	1791	174	8.8
4, [24]	Refractory	1298	1141	157	12.1	1114	184	14.1
5, [18]	Transition	175	148	27	15.5	331	156	89.1
6, [24]	Refractory	1105	1231	126	11.4	1343	238	21.5
7, [30]	Refractory	1841	1537	304	16.5	1489	352	19.1
8, [36]	Transition	655	536	119	18.2	617	38	5.8

* Measured yield strength. ** Predicted yield strength.

3.2. Evaluation Predicting Accuracy of Lasso Linear Models

Figure 4 shows the prediction results of the lasso linear model for eight test data. The mean error of yield strength was 31.1%. The mean difference was 233 MPa, and the coefficient of determination was 0.8475. The number of independent variables used in the lasso regression model was 28. The hot rolling rate and forge data's weights were zero from a total of 30 independent variables. The lasso linear regression model predicted yield strength as 14% of accuracy for 36 training data but showed low accuracy for the eight test data. When new HEA data were input, the output would be low accuracy. Thus, this model cannot be used as a prediction model. Although lasso linear regression is a more improved model than conventional linear regression, it had an error when predicting the yield strength of HEA. The mechanical properties of HEA cannot be expressed as simply linear regression. The HEA model has complex interaction by atomic radius, valance electron concentration, and shear modulus.

Figure 5 shows the results of the lasso linear model trained by only mole fraction data. The mean error was 26.1%. The mean difference was 233 MPa, and the coefficient of determination was 0.8363. Compared with the results in Figure 4, the model trained by mole fraction information showed higher accuracy than the model trained by the mole fraction and post-process data to predict the mechanical properties of HEA. This result is contrary to the prediction result of the ANN model. As the many numbers of independent variables increased, the inaccuracy of the calculation result was also increasing. Due to this feature of the linear regression method, it was difficult to express complex data in a linear model. Despite imposing a lasso penalty that made the insignificant independent variable zero, the lasso linear model with a few independent variables of the only mole fraction was

more accurate. The yield strength prediction results of eight test data calculated from both lasso linear models are given in Table 5.
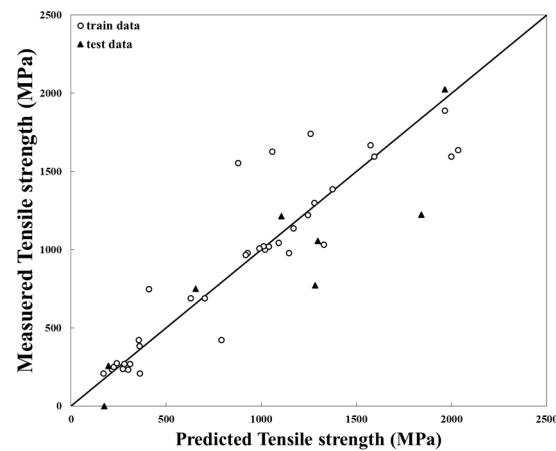

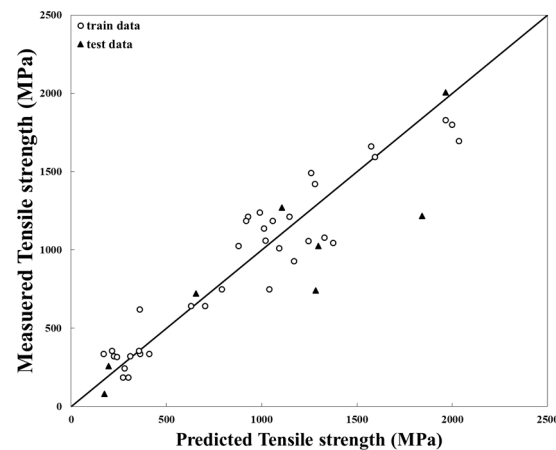**Figure 4.** Accuracy of a lasso model trained with elemental mole fraction and process data.

Figure 5. Accuracy of a lasso model trained only on elemental mole fractions.

Table 5. Comparison of the predicted results data calculated by the lasso linear model, which was trained by post-process and mole fraction data vs. mole fraction data.

No., [Ref]	HEA Group	σ_y^m * (MPa)	Lasso 1st Model Trained from Post-Process and Mole Fraction			Lasso 1st Model Trained from Mole Fraction		
			σ_y^p ** (MPa)	Error (MPa)	Error Rate (%)	σ_y^p ** (MPa)	Error (MPa)	Error Rate (%)
1, [35]	Transition	1284	773	511	39.8	742	542	42.2
2, [25]	Transition	197	256	59	30.0	257	60	30.6
3, [26]	Refractory	1965	2024	59	3.0	2007	41.5	2.1
4, [24]	Refractory	1298	1056	242	18.6	1026	273	21.0
5, [18]	Transition	175	0	175	100.0	81	94	53.8
6, [24]	Refractory	1105	1213	108	9.7	1271	166	15.0
7, [30]	Refractory	1841	1223	618	33.6	1217	624	33.9
8, [36]	Transition	655	750	95	14.5	722	67	10.2

* Measured yield strength. ** Predicted yield strength.

3.3. Effect of Process Input Data on Transition Metals and Refractory Metals

In Table 4, when the results of the refractory metal group and the transition metal group were calculated separately, the results accuracy calculated from a model trained by mole fraction and post-process information was higher than that of the model trained by only mole fraction. The transition metal group improved the accuracy by 25.0% from 52.0%

to 27.0%. The refractory metal group improved the accuracy by 1.9% from 15.9% to 14.0%. In particular, the transition metal showed significant improvement. The characteristic of the transition metal group is basically a group with a low yield strength. Yield strength is largely changed according to post-treatment process conditions. To get higher prediction accuracy of the transition metal group, post-process information that has more effect on the mechanical properties was important. When post-process information is more detailed, such as at a big data level, the accuracy of the prediction model is likely to improve. The lasso prediction results in Table 5 showed the opposite results to the ANN prediction results. In the transition metal group, the error rate of the model trained only with the mole fraction was 34%, and the model trained with the post-process showed an error rate of 46%, which actually decreased the accuracy by 12%. Similarly, the refractory metal group showed a 2% reduction in error rate from 18% to 16%. This result also reflected the character of the linear regression equation through which the prediction accuracy decreases as the number of variables increases.

3.4. Assessment of the Influence of Elements in Alloys

Figure 6 shows the coefficient ratio of each variable in the lasso regression analysis derived from only element data. The absolute value of the coefficient is expressed as a percentage, and the coefficient having a negative value is indicated as a minus in the variable name. It is correct to derive the model by dividing the transition and refractory groups, but since the elements included in the alloy are often manufactured by mixing them, they were used as input data without classifying all elements. Mn and W are not indicated because the coefficients are 0, as the characteristics of the lasso regression analysis make the coefficients 0 if there is no influence. Elements that had a positive effect on strength were Al, Mo, Zr, Ti, Ta, Cu, and Cr, whereas elements that had a negative effect were V, Nb, Hf, Ni, Co, and Fe.
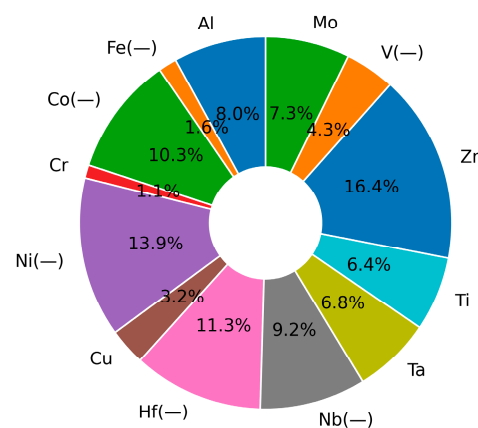
Figure 6. Influence of coefficients in the lasso regression model.

Table 6 shows the effect of the change of each variable value on the yield strength in the ANN model derived from elemental data and process data. These data are obtained by calculating the value that changes when 1 is increased in the normalized data. It is similar to the coefficient value of each variable derived from lasso regression. Unlike lasso regression, the effect of the same element on the 44 data used for training and testing each piece of data is different for each piece of data. Due to the nature of the neural network, each and every datum has an effect on all nodes, resulting in a yield strength value, so the correlation between input variables is strong. Elements that had a positive influence on strength were Al, Cr, Cu, Nb, Ta, Ti, Zr, Mo, and W, whereas elements that had a negative influence were Co, Fe, Ni, Mn, Hf, and V. Compared with the lasso regression analysis, only Nb elements showed different results, but other elements showed the same results. In Table 6, the ratio of whether the effect of a specific element on the yield strength is positive or negative for each data is shown. The effect of each element on the yield strength of

the alloy was confirmed similarly, but the ANN model shows higher accuracy because it reflects the different correlations due to different elements and post-process for each data. In the case of Cr, the yield strength increased as the amount of Cr increased in most HEAs, but the 28 AlCoCrCuFeNi and eight Al0.5CoCrCuFeNi alloys in Table 6 resulted in a decrease in yield strength. This was the result of a complex causal relationship.

Table 6. Yield strength prediction data set that changes when the input data increases by 1.

No., [Ref]	Alloy	Al	Co	Cr	Fe	Ni	Cu	Mn	Hf	Nb	Ta	Ti	Zr	V	Mo	W
		Yield Strength Increase per 1 Increase in Input Data														
1, [9] *	NbCrMo$_{0.5}$Ta$_{0.5}$TiZr	245	−83	195	−193	−107	119	−166	−346	348	153	609	810	−331	338	658
2, [14]	Al$_{0.5}$CoCrCu$_{0.5}$FeNi$_2$	155	−5	111	−107	−17	99	−113	−167	242	68	405	598	−161	199	451
3, [15]	Al$_{0.5}$CoCrCuFeNi	231	−26	179	−134	−43	109	−92	−220	332	137	596	796	−228	323	644
4, [16]	AlNbTiV	236	−89	186	−199	−113	111	−171	−352	339	144	600	801	−337	329	649
5, [9]	NbCrMo$_{0.5}$Ta$_{0.5}$TiZr	414	90	362	−2	85	286	35	−138	515	320	779	979	−136	506	828
6, [18]	Al$_{0.5}$NbTaTiV	255	−70	205	−181	−94	130	−152	−333	358	163	619	819	−319	348	667
7, [19]	CoCrFeNi	175	−32	162	−134	−43	104	−146	−211	267	100	494	694	−204	261	544
8, [20]	AlCoCrCuFeNi	238	−87	188	−197	−111	113	−170	−350	341	146	602	803	−335	331	651
9, [21]	Al$_{0.3}$CoCrFeNi	199	−9	164	−111	−22	104	−81	−166	299	113	564	764	−159	291	613
10, [22]	MoNbTaVW	235	−90	185	−201	−114	110	−172	−353	338	143	599	799	−339	328	647
11, [23]	Al$_{0.5}$CrCuFeNi$_2$	237	−78	187	−198	−115	111	−175	−319	339	144	601	802	−312	330	650
12, [24]	CrHfNbTiZr	260	−65	211	−175	−88	135	−147	−327	364	169	624	825	−313	353	673
13, [21]	Al$_{0.3}$CoCrFeNi	213	−45	161	−147	−57	86	−125	−240	314	119	578	778	−236	305	626
14, [25]	NbTiVZr	254	−43	202	−136	−48	127	−98	−272	355	160	619	819	−270	346	668
15, [26]	CrCrFeMnNi	200	−3	186	−99	−15	117	−76	−143	305	135	543	743	−141	299	594
16, [27]	Al$_{0.3}$NbTaTi$_{1.4}$Zr$_{1.3}$	62	−265	13	−375	−289	−62	−348	−528	166	−29	426	627	−513	155	475
17, [21]	Al$_{0.3}$CoCrFeNi	258	14	206	−88	3	130	−70	−177	359	164	622	823	−172	350	671
18, [19]	CoCrMnNi	188	−41	174	−151	−59	105	−112	−222	293	123	522	722	−214	287	573
19, [18]	AlNbTaTiV	297	−28	247	−139	−52	172	−110	−291	400	205	660	861	−277	389	709
20, [24]	HfNbTiVZr	148	−177	98	−288	−201	23	−260	−441	251	56	512	712	−426	241	560
21, [28]	HfNbTaTiZr	344	14	292	−96	−10	216	−69	−249	445	250	708	909	−234	436	757
22, [26]	CoCrFeMnNi	11	−187	−3	−286	−198	−72	−263	−332	116	−54	359	559	−331	110	409
23, [25]	CrNbTiZr	747	419	698	309	395	622	336	156	850	655	1111	1312	171	840	1160
24, [29]	CoCrFeNi	52	−119	29	−199	−116	−15	−181	−249	152	−21	395	595	−236	143	445
25, [30]	AlMo$_{0.5}$NbTa$_{0.5}$TiZr	−127	−454	−177	−564	−478	−252	−537	−717	−24	−219	237	437	−702	−34	285
26, [31]	HfMoNbTiZr	−38	−363	−88	−474	−387	−163	−445	−626	65	−130	326	526	−612	55	374
27, [32]	CrMnFeCoNi	524	199	472	84	170	396	111	−53	625	430	887	1088	−54	616	936
28, [20]	AlCoCrCuFeNi	−125	−410	−176	−521	−428	−252	−478	−613	−24	−219	239	440	−627	−32	288
29, [23]	Al$_{0.5}$CrCuFeNi$_2$	315	−3	264	−122	−38	189	−97	−246	417	222	679	879	−237	408	727
30, [27]	Al$_{0.5}$NbTa$_{0.8}$Ti$_{1.5}$V$_{0.2}$Zr	−172	−499	−221	−609	−523	−296	−582	−762	−68	−263	192	393	−747	−79	241
31, [18]	Al$_{0.25}$NbTaTiV	−75	−400	−125	−510	−424	−200	−483	−663	28	−167	289	489	−648	18	337
32, [14]	Al$_{0.5}$CoCrCu$_{0.5}$FeNi$_2$	125	−95	81	−197	−106	24	−157	−270	226	31	490	690	−277	217	539
33, [33]	HfNbTiZr	713	388	664	278	364	589	305	125	817	622	1077	1278	140	806	1126
34, [22]	MoNbTaW	872	547	822	437	523	747	465	284	975	780	1236	1436	299	965	1284
35, [34]	NbTaTiV	150	−175	101	−285	−199	25	−258	−438	254	59	514	715	−423	243	563
36, [27]	AlNb$_{1.5}$Ta$_{0.5}$Ti$_{1.5}$Zr$_{0.5}$	466	139	417	29	115	342	56	−118	570	375	830	1031	−109	559	879
1t**, [35]	Al$_{0.5}$CoCrCuFeNi	−618	−847	−640	−968	−878	−705	−965	−1071	−518	−691	−254	−54	−1075	−526	−206
2t, [26]	CrCrFeMnNi	175	−26	161	−124	−38	92	−100	−169	279	110	520	720	−167	274	571
3t, [27]	Al$_{0.3}$NbTa$_{0.8}$Ti$_{1.4}$V$_{0.2}$Zr$_{1.3}$	5	−322	−44	−432	−346	−119	−405	−585	109	−86	369	570	−570	98	418
4t, [25]	CrNbTiVZr	193	−137	141	−247	−161	65	−220	−400	294	99	557	758	−385	285	606
5t, [19]	CoFeMnNi	−2	−144	−46	−157	−124	−54	−146	−157	97	−74	258	439	−157	54	318
6t, [25]	NbTiVZr	505	176	454	66	152	379	95	−78	607	412	869	1070	−72	598	918
7t, [30]	Al$_{0.4}$Hf$_{0.6}$NbTaTiZr	−308	−638	−360	−749	−662	−436	−716	−889	−208	−403	55	256	−886	−216	104
8t, [36]	Al$_{0.5}$CoCrCuFeNi	4	−225	−18	−346	−256	−83	−341	−447	105	−69	368	569	−453	96	417
Positive effect ratio (%)		82	20	75	14	18	70	16	7	89	70	98	98	7	89	98

No., [Ref]	Heat Treatment 1		Cooling		CR	HR		Heat Treatment 2		Forge	HIP			Heat Treatment 3	
	Temp (°C)	h	WQ	SC	CR (%)	Temp (°C)	HR (%)	Temp (°C)	h	Forge	Temp (°C)	Press (MPa)	h	Temp (°C)	h
														Post−Process Input Data	
1, [9]	−142	190	−104	9	153	56	8	−12	301	609	−39	−38	−77	−56	−1595
2, [14]	−63	86	−2	5	115	51	−8	−25	195	398	−20	−40	−55	6	−215
3, [15]	−90	175	−29	15	151	55	10	−8	285	595	−30	−41	−50	−9	−360
4, [16]	−148	181	−110	1	144	48	2	−20	292	600	−47	−45	−83	−62	−1020
5, [9]	31	358	73	175	320	223	175	155	468	778	133	129	112	136	−929
6, [18]	−129	199	−91	19	162	67	20	−2	311	618	−28	−26	−64	−43	−1012
7, [19]	−90	123	−29	4	156	29	−4	2	249	493	−47	−59	−82	−21	−273
8, [20]	−146	183	−108	3	146	50	4	−18	294	602	−45	−43	−81	−60	−1040
9, [21]	−69	143	−8	16	137	54	6	−18	253	563	−26	−34	−46	0	−224
10, [22]	−149	179	−111	−1	142	47	0	−22	291	598	−48	−46	−84	−63	−1246
11, [23]	−141	182	−86	0	144	48	0	−21	293	601	−48	−47	−86	−64	−704
12, [24]	−124	205	−85	25	168	73	26	4	316	624	−22	−21	−58	−38	−1375
13, [21]	−103	158	−42	−12	124	38	−18	−31	268	577	−46	−60	−68	−34	−310
14, [25]	−103	198	−60	16	160	85	16	−5	308	619	−1	−13	−21	3	−918
15, [26]	−62	145	−1	23	163	57	18	9	265	543	−19	−31	−35	7	−171
16, [27]	−323	7	−285	−173	−30	−125	−173	−194	118	426	−221	−220	−259	−238	−1965
17, [21]	−44	202	17	37	177	88	31	23	312	622	8	−10	−18	25	−240
18, [19]	−106	133	−45	12	148	32	6	−11	253	522	−49	−56	−68	−24	−280
19, [18]	−87	241	−49	61	204	109	62	40	353	660	14	15	−22	−1	−991
20, [24]	−236	92	−198	−87	55	−40	−87	−108	204	511	−135	−133	−172	−150	−1170
21, [28]	−45	288	−7	105	250	153	105	85	398	708	58	59	20	41	−1145
22, [26]	−245	−44	−184	−163	−29	−124	−171	−183	76	358	−202	−212	−220	−176	−362
23, [25]	361	692	399	511	655	559	511	490	803	1111	463	464	425	447	−1260
24, [29]	−159	−12	−117	−104	13	−64	−94	−127	109	394	−128	−132	−136	−109	−300

Table 6. *Cont.*

No., [Ref]	Heat Treatment 1		Cooling		CR	HR		Heat Treatment 2		Forge	HIP			Heat Treatment 3	
	Temp (°C)	h	WQ	SC	CR (%)	Temp (°C)	HR (%)	Temp (°C)	h	Forge	Temp (°C)	Press (MPa)	h	Temp (°C)	h
25, [30]	−513	−183	−475	−363	−220	−315	−363	−384	−71	236	−410	−409	−448	−427	−2000
26, [31]	−422	−94	−384	−274	−131	−226	−273	−295	18	325	−321	−319	−357	−336	−1575
27, [32]	135	468	178	285	430	333	285	264	578	887	238	239	199	221	−410
28, [20]	−481	−180	−420	−358	−218	−310	−363	−381	−70	239	−395	−408	−415	−391	−790
29, [23]	−65	260	−12	78	222	126	78	57	371	678	30	31	−8	14	−630
30, [27]	−557	−227	−519	−407	−264	−359	−407	−428	−115	192	−455	−454	−493	−472	−2035
31, [18]	−459	−130	−421	−310	−168	−263	−309	−331	−19	289	−358	−356	−394	−373	−1330
32, [14]	−153	69	−92	−65	54	−26	−74	−104	179	489	−108	−115	−126	−83	−357
33, [33]	329	658	368	478	621	526	479	457	769	1077	431	432	394	415	−879
34, [22]	488	817	526	637	779	684	638	616	928	1236	589	591	553	574	−1058
35, [34]	−234	95	−195	−85	58	−37	−84	−106	206	514	−132	−131	−169	−148	−1092
36, [27]	80	411	119	231	374	279	230	210	523	830	183	184	145	167	−1280
1t, [35]	−905	−674	−849	−803	−653	−780	−809	−807	−560	−255	−862	−868	−914	−856	−1284
2t, [26]	−85	120	−24	−2	137	35	−7	−17	240	520	−41	−53	−58	−16	−197
3t, [27]	−380	−50	−342	−230	−87	−182	−230	−251	62	369	−278	−277	−316	−295	−1965
4t, [25]	−196	137	−158	−45	99	3	−46	−66	247	557	−93	−92	−132	−110	−1298
5t, [19]	−146	−71	−142	−130	−41	−101	−127	−132	38	244	−131	−127	−133	−138	−175
6t, [25]	117	450	156	268	412	316	267	247	560	869	220	221	182	203	−1105
7t, [30]	−697	−364	−659	−547	−403	−499	−547	−568	−254	55	−595	−594	−633	−611	−1841
8t, [36]	−283	−51	−227	−181	−31	−158	−186	−185	62	368	−239	−246	−292	−234	−655
Ratio (%)	16	73	18	55	73	64	50	32	86	98	25	23	18	32	0

* reference number. ** test data.

In TiZrHfNbX (X = V or Cr) HEA, the yield strength was increased when the Cr element was added instead of the V element [28]. The fact that the V element lowers the yield strength was similar to the conclusion calculated from the ANN and lasso model. In addition, the effect of Al on Al CoCrFeNi HEA was found to be positive. At low Al content, the alloys form FCC structures. When the Al amount is continuously increased, the formation of the BCC phase has been induced. It also increases the strength of the HEA with a modulated spinodal structure. The complete spinodal structure can be obtained in amounts of Al0.9-2.0. The cast Al0.9 alloy has a maximum hardness of HV 527 due to the optimal radial decomposition and interconnecting structure [38]. Positively affecting elements such as Al had the same positive effects on other HEAs. In addition, elements such as Fe, Ni, and Co also had a negative effect on other alloys.

In the post-process data of Table 6, the size of the data set is small, and inaccurate results are often shown. The HIP process reduces the tensile strength due to grain coarsening in AlxCoCrFeNi alloy of the transition metal group [39]. Table 6 also shows that hot isostatic pressing has a negative effect on yield strength. However, similar to other heat treatment temperatures, it is difficult to obtain accurate and detailed results because the experimental data by temperature or time conditions are not trained. In the case of trend prediction, cold rolling and forge were confirmed as variables to improve the tensile strength. This process is known to increase the yield strength of metals through work hardening. In the case of heat treatment, the result was that the tensile strength decreased as the temperature increased and the tensile strength increased with time. This result is also difficult to be trusted due to the lack of heat treatment data, and more accurate results can be obtained when more data are collected in the future.

4. Conclusions

In this paper, a new methodology for predicting the mechanical properties of HEA is proposed. The design of HEA is complicatedly entangled with material theories including thermodynamic and physical relationships between constituent elements and post-processing. To approach this process efficiently, the mechanical properties of the

alloy were predicted using only the mole fraction and post-process data using the ANN algorithm. The main results are as follows:

1. The ANN prediction model showed high accuracy only when learning the post-process data together; the tensile strength showed an error rate of 19.7%, and the microstructure was consistent in all test data. Elongation prediction showed a high error rate of 40.2%.

2. In the case of the lasso linear regression, the error rate of the model trained with post-processing data was 31.1%, and the error rate of the lasso model trained only on the mole fraction was 26.1%, showing low accuracy. The linear regression model did not sufficiently reflect the complex causal relationships in the data as the variable increased.

3. When post-process data were trained with the element mole fraction, the model error rate decreased from 15.9% to 14% in the refractory metal group, and the error rate of the transition metal group decreased from 52% to 27% in the transition metal group. In contrast, the lasso model showed the opposite trend.

4. In the ANN model, Al, Cr, Cu, Nb, Ta, Ti, Zr, Mo, and W increased the strength as these components increased, and Co, Fe, Ni, Mn, Hf, and V decreased the tensile strength. In the lasso model, the same results were obtained except for Nb. In addition, in the post-process, cold rolling and forging improved the tensile strength.

Author Contributions: Conceptualization, S.C.; methodology, S.C.; software, S.C.; validation, S.Y. and B.S.; formal analysis, J.K.; investigation, S.C.; writing—original draft preparation, S.C.; writing—review and editing, S.H.; supervision, S.Y. All authors have read and agreed to the published version of the manuscript.

Institutional Review Board Statement: Not applicable.

Informed Consent Statement: Not applicable.

Data Availability Statement: Data available on request from the authors.

Conflicts of Interest: The authors declare no conflict of interest.

References

1. Yeh, J.W. Alloy design strategies and future trends in high-entropy alloys. *JOM* **2013**, *65*, 1759–1771. [CrossRef]
2. Singh, S.; Wanderka, N.; Kiefer, K.; Siemensmeyer, K.; Banhart, J. Effect of decomposition of the Cr-Fe-Co rich phase of AlCoCrCuFeNi high entropy alloy on magnetic properties. *Ultramicroscopy* **2011**, *111*, 619–622. [CrossRef]
3. Gao, M.C.; Zhang, B.; Guo, S.M.; Qiao, J.W.; Hawk, J.A. High-entropy alloys in hexagonal close-packed structure. *Metall. Mater. Trans. A* **2016**, *47*, 3322–3332. [CrossRef]
4. Zhang, C.; Zhang, F.; Chen, S.; Cao, W. Computational thermo.dynamics aided high-entropy alloy design. *JOM* **2012**, *64*, 839–845. [CrossRef]
5. Domìnguez, L.A.; Goodall, R.; Todd, I. Prediction and validation of quaternary high entropy alloys using statistical approaches. *Mater. Sci. Technol.* **2015**, *31*, 1201–1206.
6. Senkov, O.N.; Miller, J.D.; Miracle, D.B.; Woodward, C. Accelerated exploration of multi-principal element alloys for structural applications. *Calphad* **2015**, *50*, 32–48. [CrossRef]
7. Tazuddin; Gurao, N.P.; Biswas, K. In the quest of single phase multi-component multiprincipal high entropy alloys. *J. Alloy. Compd.* **2017**, *697*, 434–442. [CrossRef]
8. Xie, L.; Brault, P.; Thomann, A.L.; Bauchire, J.M. AlCoCrCuFeNi high entropy alloy cluster growth and annealing on silicon: A classical molecular dynamics simulation study. *Appl. Surf. Sci.* **2013**, *285*, 810–816. [CrossRef]
9. Senkov, O.N.; Woodward, C.F. Microstructure and properties of a refractory $NbCrMo_{0.5}Ta_{0.5}TiZr$ alloy. *Mater. Sci. Eng. A* **2011**, *529*, 311–320. [CrossRef]
10. Osintsev, K.; Konovalov, S.; Gromov, V.; Panchenko, I.; Chen, X. Phase composition prediction of Al-Co-Cr-Fe-Ni high entropy alloy system based on thermodynamic and electronic properties calculations. *Mater. Today Proc.* **2021**, *46*, 961–965. [CrossRef]

11. Manzoor, A.; Aidhy, D.S. Predicting vibrational entropy of fcc solids uniquely from bond chemistry using machine learning. *Materialia* **2020**, *46*, 961–965. [CrossRef]

12. Zhang, Y.; Wen, C.; Wang, C.; Antonov, S.; Xue, D.; Bai, Y.; Su, Y. Phase prediction in high entropy alloys with a rational selection of materials descriptors and machine learning models. *Acta Mater.* **2019**, *185*, 528–539. [CrossRef]

13. Pei, Z.; Yin, J.; Hawk, J.A.; Alman, D.E.; Gao, M.C. Machine-learning informed prediction of high-entropy solid solution formation: Beyond the Hume-Rothery rules. *Comput. Mater.* **2020**, *6*, 50. [CrossRef]

14. Daoud, H.M.; Manzoni, A.; Volkl, R.; Wanderka, N.; Glatzel, U. Microstructure and tensile behavior of $Al_{18}Co_{17}Cr_{17}Cu_8Fe_{17}Ni_{33}$ (at.%) high-entropy alloy. *JOM* **2013**, *65*, 1805–1814. [CrossRef]

15. Wang, F.J.; Zhang, Y.; Chen, G.L.; Davies, H.A. Tensile and compressive mechanical behavior of a $CoCrCuFeNiAl_{0.5}$ high entropy alloy. *Int. J. Mod. Phys. B* **2009**, *23*, 1254–1259. [CrossRef]

16. Stepanov, N.D.; Shaysultanov, D.G.; Salishchev, G.A.; Tikhonovsky, M.A. Structure and mechanical properties of a light-weight AlNbTiV high entropy alloy. *Mater. Lett.* **2015**, *142*, 153–155. [CrossRef]

17. Senkov, O.N.; Scott, J.M.; Senkova, S.V.; Meisenkothen, F.; Miracle, D.B.; Woodward, C.F. Microstructure and elevated temperature properties of a refractory TaNbHfZrTi alloy. *J. Mater. Sci.* **2012**, *47*, 4062–4074. [CrossRef]

18. Yang, X.; Zhang, Y.; Liaw, P.K. Microstructure and compressive properties of NbTiVTaAlx high entropy alloys. *Procedia Eng.* **2012**, *36*, 292–298. [CrossRef]

19. Wu, Z.; Bei, H.; Pharr, G.M.; George, E.P. Temperature dependence of the mechanical properties of equiatomic solid solution alloys with face-centered cubic crystal structures. *Acta Mater.* **2014**, *81*, 428–441. [CrossRef]

20. Kuznetsov, A.V.; Shaysultanov, D.G.; Stepanov, N.D.; Salishchev, G.A.; Senkov, O.N. Tensile properties of an AlCrCuNiFeCo high-entropy alloy in ascast and wrought conditions. *Mater. Sci. Eng. A* **2012**, *533*, 107–118. [CrossRef]

21. Shun, T.T.; Du, Y.C. Microstructure and tensile behaviors of FCC $Al_{0.3}CoCrFeNi$ high entropy alloy. *J. Alloy. Compd.* **2009**, *479*, 157–160. [CrossRef]

22. Senkov, O.N.; Wilks, G.B.; Scott, J.M.; Miracle, D.B. Mechanical properties of $Nb_{25}Mo_{25}Ta_{25}W_{25}$ and $V_{20}Nb_{20}Mo_{20}Ta_{20}W_{20}$ refractory high entropy alloys. *Intermetallics* **2011**, *19*, 698–706. [CrossRef]

23. Ng, C.; Guo, S.; Luan, J.; Wang, Q.; Lu, J.; Shi, S.; Liu, C.T. Phase stability and tensile properties of Co-free $Al_{0.5}CrCuFeNi_2$ high-entropy alloys. *J. Alloy. Compd.* **2014**, *584*, 530–537. [CrossRef]

24. Fazakas, E.; Zadorozhnyy, V.; Varga, L.K.; Inoue, A.; Louzguine-Luzgin, D.V.; Tian, F.; Vitos, L. Experimental and theoretical study of $Ti_{20}Zr_{20}Hf_{20}Nb_{20}X_{20}$ ($X \frac{1}{4}$ V or Cr) refractory high-entropy alloys. *Int. J. Refract. Met. Hard Mater.* **2014**, *47*, 131–138. [CrossRef]

25. Senkov, O.N.; Senkova, S.V.; Miracle, D.B.; Woodward, C. Mechanical properties of low-density, refractory multi-principal element alloys of the Cr–Nb–Ti–V–Zr system. *Mater. Sci. Eng. A* **2013**, *565*, 51–62. [CrossRef]

26. Otto, F.; Dlouhy, A.; Somsen, C.; Bei, H.; Eggler, G.; George, E.P. The influences of temperature and microstructure on the tensile properties of a CoCrFeMnNi high-entropy alloy. *Acta Mater.* **2013**, *61*, 5743–5755. [CrossRef]

27. Senkov, O.N.; Woodward, C.; Miracle, D.B. Microstructure and properties of aluminum-containing refractory high-entropy alloys. *JOM* **2014**, *66*, 2030–2042. [CrossRef]

28. Senkovab, O.N.; Semiatina, S.L. Microstructure and properties of a refractory high-entropy alloy after cold working. *J. Alloy. Compd.* **2015**, *649*, 1110–1123. [CrossRef]

29. Galiab, A.; Georgeab, E.P. Tensile properties of high- and medium-entropy alloys. *Intermetallics* **2013**, *39*, 74–78.

30. Senkov, O.N.; Senkova, S.V.; Woodward, C. Effect of aluminum on the microstructure and properties of two refractory high entropy alloys. *Acta Mater.* **2014**, *68*, 214–228. [CrossRef]

31. Guo, N.N.; Wang, L.; Luo, L.S.; Li, X.Z.; Su, Y.Q.; Guo, J.J.; Fu, H.Z. Microstructure and mechanical properties of refractory MoNbHfZrTi high-entropy alloy. *Mater. Des.* **2015**, *81*, 87–94. [CrossRef]

32. Gludovatz, B.; Hohenwarter, A.; Catoor, D.; Chang, E.H.; George, E.P.; Ritchie, R.O. A fracture-resistant high-entropy alloy for cryogenic applications. *Science* **2014**, *345*, 1153–1158. [CrossRef] [PubMed]

33. Wu, Y.D.; Cai, Y.H.; Wang, T.; Si, J.J.; Zhu, J.; Wang, Y.D.; Hui, X.D. A refractory $Hf_{25}Nb_{25}Ti_{25}Zr_{25}$ high-entropy alloy with excellent structural stability and tensile properties. *Mater. Lett.* **2014**, *130*, 277–280. [CrossRef]

34. Yang, X.; Zhang, Y. Prediction of high-entropy stabilized solid-solution in multicomponent alloys. *Mater. Chem. Phys.* **2012**, *132*, 233–238. [CrossRef]

35. Hemphilla, M.A.; Yuanb, T.; Wanga, G.Y.; Yehc, J.W.; Tsaic, C.W.; Chuanga, A.; Liawa, P.K. Fatigue behavior of $Al_{0.5}CoCrCuFeNi$ high entropy alloys. *Acta Mater.* **2012**, *60*, 5723–5734. [CrossRef]

36. Tsai, C.W.; Tsai, M.H.; Yeh, J.W.; Yang, C.C. Effect of temperature on mechanical properties of $Al_{0.5}CoCrCuFeNi$ wrought alloy. *J. Alloy. Compd.* **2010**, *49*, 160–165. [CrossRef]

37. Diederik, P.K.; Jimmy, L.B. ADAM: A Method For Stochastic Optimization. *arXiv* **2014**, arXiv:1412.6980.

38. Wang, W.R.; Wang, W.L.; Wang, S.C.; Tsai, Y.C.; Lai, C.H.; Yeh, J.W. Effects of Al addition on the microstructure and mechanical property of AlxCoCrFeNi high-entropy alloys. *Intermetallics* **2012**, *26*, 44–51. [CrossRef]

39. Joseph, J.; Hodgsona, P.; Jarvisb, T.; Wub, X.; Stanfordc, N.; Fabijanica, D.K. Effect of hot isostatic pressing on the microstructure and mechanical properties of additive manufactured AlxCoCrFeNi high entropy alloys. *Mater. Sci. Eng. A* **2018**, *733*, 59–70. [CrossRef]